J. Fluid Mech. (2000), *vol.* 418, *pp.* 213–229. Printed in the United Kingdom

Analysis and direct numerical simulation of the flow at a gravity-current head. Part 2. The lobe-and-cleft instability

By CARLOS HÄRTEL, FREDRIK CARLSSON AND MATTIAS THUNBLOM†

ETH, Institute of Fluid Dynamics, ETH Zentrum, CH-8092 Zürich, Switzerland

(Received 28 September 1999 and in revised form 11 April 2000)

Results are presented from a linear-stability analysis of the flow at the head of two-dimensional gravity-current fronts. The analysis was undertaken in order to clarify the instability mechanism that leads to the formation of the complex lobe-and-cleft pattern which is commonly observed at the leading edge of gravity currents propagating along solid boundaries. The stability analysis concentrates on the foremost part of the front, and is based on direct numerical simulation data of two-dimensional lock-exchange flows which are described in the companion paper, Härtel *et al.* (2000). High-order compact finite differences are employed to discretize the stability equations which results in an algebraic eigenvalue problem for the amplification rate, that is solved in an iterative fashion. The analysis reveals the existence of a vigorous linear instability that acts in a localized way at the leading edge of the front and originates in an unstable stratification in the flow region between the nose and stagnation point. It is shown that the amplification rate of this instability as well as its spanwise length scale depend strongly on Reynolds number. For validation, three-dimensional direct numerical simulations of the early stages of the frontal instability are performed, and close agreement with the results from the linear-stability analysis is demonstrated.

1. Introduction

Gravity currents spreading along solid boundaries typically feature an intense three-dimensional motion at the leading edge that is accompanied by a substantial entrainment of light fluid into the gravity-current head (cf. Britter & Simpson 1978; Hallworth *et al.* 1996). Many experiments have shown that the flow in this region is composed of a complex pattern of so-called lobes and clefts which are highly unsteady and continuously shift along the leading edge (Simpson 1997). This intriguing feature of gravity-current fronts could also be observed in the three-dimensional direct numerical simulation (DNS) of a lock-exchange flow which we discussed and analysed in Part 1 of the present study (Härtel, Meiburg & Necker 2000). A snapshot of the flow at the head obtained from this simulation is given in figure 1, where the flow field is visualized by an isosurface of density. Around the leading edge, the isosurface is highly distorted, and its shape reveals the existence of distinct lobes which closely resemble those observed in laboratory experiments (see, for example, figure 1 of Simpson 1969).

† Permanent address: Department of Thermo- and Fluid Dynamics, Chalmers University of Technology, Göteborg, Sweden.

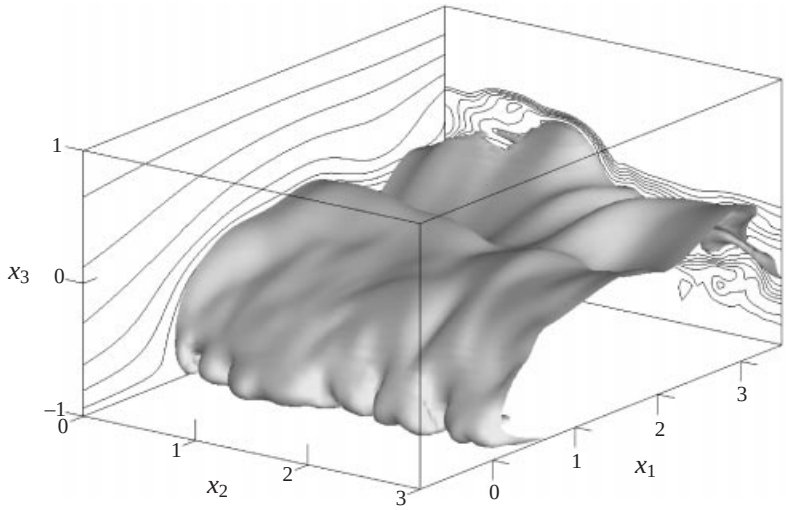

FIGURE 1. Structure of the foremost part of a gravity current in a three-dimensional DNS simulation of lock-exchange flow. The Reynolds number, based on height and propagation speed of the front, is about 750. The front structure is visualized by a density isosurface ($\rho = 0.5$). Side-plane: instantaneous streamlines in a frame of reference moving with the front. Back plane: density distribution.

The omni-presence of the lobe-and-cleft structure strongly suggests that it originates in some fundamental and vigorous instability, but the driving mechanism behind it has not been fully clarified. Most of what is known to date about this phenomenon still traces back to the work of Simpson (1972) who studied aspects of the lobe formation over a wide range of Reynolds numbers. His experiments revealed the importance of buoyancy forces for the occurrence of the lobes and clefts, and highlighted the influence of the conditions at the wall along which the front spreads. From Simpson's observations it was conjectured that a gravitational rise of the thin layer of light fluid that the gravity current overruns is responsible for the breakdown of the flow front at the leading edge. Simpson employed different techniques to avoid near-wall light fluid becoming trapped underneath the front, and found that the lobe formation at the leading edge indeed disappeared. However, no sufficiently detailed measurements were available to disclose details of structure and location of the frontal instability, and consequently the actual involvement of the potentially unstable light fluid underneath the head remained unresolved.

To examine the hydrodynamic instability behind the lobe-and-cleft structure, we have undertaken a stability analysis of the flow at the head of a gravity current. In this analysis we do not address the dynamics of fully developed lobes directly, but rather approach the problem by looking at two-dimensional fronts, trying to clarify whether or not they are unstable to small three-dimensional disturbances. Our aim is to identify the primary and three-dimensional linear instability that drives an initially two-dimensional flow front into a three-dimensional state. The appearance of this primary instability, as observed in experiments, is sketched in figure 2. It is seen that the transition to a three-dimensional flow is accompanied by the formation of a regular structure of filaments which persist for some distance downstream before collapsing into the more irregular pattern of shifting lobes and clefts. As pointed out by Simpson (1972), these filaments indicate the existence of an initially preferred lobe size which presumably corresponds to the wavelength of some most unstable

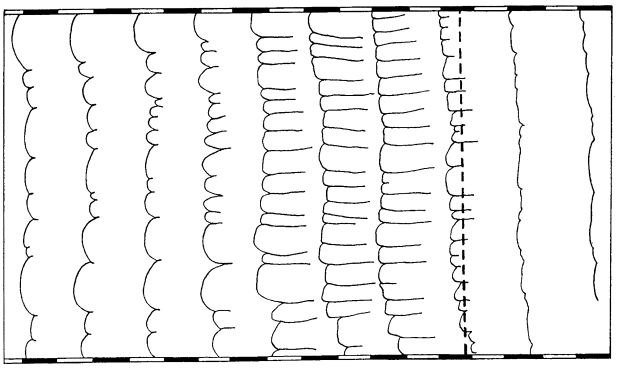

FIGURE 2. Initiation of the lobe-and-cleft structure at the head of a gravity current as observed in the experiments of Simpson (1972). Plan view at intervals of $\frac{1}{3}$ s. The flow is from right to left at a Reynolds number of about 4500 ($Gr \approx 4 \times 10^7$). Initially, the floor underneath the front was moved with the front giving an almost two-dimensional flow structure at the leading edge. At the position of the dashed vertical line the floor was suddenly brought to rest. The rapid transition to a filamentary structure, which precedes the final breakdown into the lobes and clefts, is clearly recognized.

mode. The sketch makes clear that the filaments start to form at the leading edge of the front. This is in accordance with a finding discussed in Part 1, namely that the breakdown of a two-dimensional flow front becomes visible first at the foremost part and appears in the form of sinusoidal disturbances. These observations suggest that the two-dimensional/three-dimensional transition at the head is caused by an instability that acts locally at the leading edge, rather than by a buoyancy-induced rise of light fluid that the front has overrun.

As basis for the linear-stability analysis we employ the DNS results of two-dimensional lock-exchange flows which we presented in Part 1. From the DNS, the flow at the head of the front is known with high accuracy which allows its response to small three-dimensional disturbances to be examined carefully. In the stability analysis we will focus on the flow at the foremost part of the head which we consider in a translating system moving with the front. Of special interest to us are the spatial structure and the amplification rates of the most unstable modes. In order to assess the influence of viscous forces on the frontal instability, we will study flows over a range of Reynolds numbers which extends up to about 14 000. At present, no sufficiently detailed experimental observations are available that could serve for comparison with our linear-stability results. Therefore, we have also conducted three-dimensional direct simulations of the early stages of the frontal breakdown in the course of our study for validation purposes.

2. Basic equations

In the present work we address flows driven by small density differences, which are described by the Boussinesq approximation of the incompressible Navier–Stokes equations (cf. Gebhart *et al.* 1979). The dimensionless governing equations derived in Part 1 have the form

$$\frac{\partial u_k}{\partial x_k} = 0, \tag{1}$$

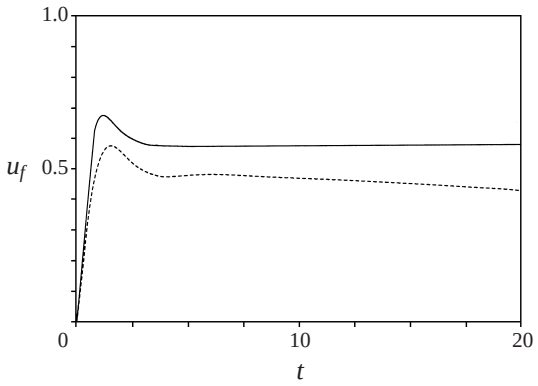

FIGURE 3. Temporal development of the non-dimensional front speed u_f after release. Results for Grashof numbers of 3×10^4 (dashed line) and 10^6.

$$\frac{\partial u_i}{\partial t} + \frac{\partial (u_i u_k)}{\partial x_k} = -\frac{\partial p}{\partial x_i} + \frac{1}{\sqrt{Gr}} \frac{\partial^2 u_i}{\partial x_k \partial x_k} + \rho e_i^g, \tag{2}$$

$$\frac{\partial \rho}{\partial t} + \frac{\partial (\rho u_k)}{\partial x_k} = \frac{1}{\sqrt{GrSc^2}} \frac{\partial^2 \rho}{\partial x_k \partial x_k}, \tag{3}$$

where the half-height $\tilde{h}$ of the lock-exchange channel and the buoyancy velocity $\tilde{u}_b$ were employed for non-dimensionalization. As in Part 1, the governing dimensionless parameters are the Grashof number Gr, which is the ratio of buoyancy forces to viscous forces, and the Schmidt number Sc. In the present stability analysis, the Schmidt number will generally be unity, whereas the Grashof number is varied between 3×10^4 and 4×10^8. Given the common definition of the Reynolds number of a gravity current by means of the actual height and speed of the head of the front (see Part 1), the Grashof-number regime examined corresponds to a range of Reynolds numbers from below 100 to about 14 000.

3. Two-dimensional base flow

Before we concentrate on the stability results in § 4, we will briefly summarize the main characteristics of the two-dimensional lock-exchange flows, which we subject to the linear-stability analysis. A detailed description of the respective DNS results was given in Part 1, where the numerical methods employed for the DNS were also discussed. The lock-exchange set-up is well suited to study the dynamics of the flow at a gravity-current head since after a short initial transient the fronts travel at essentially constant speed. This allows the head to be considered in a translating system moving with the front, in which the flow at the foremost part is stationary. This feature of the lock-exchange flow is illustrated in figure 3 where the non-dimensional speed of the front is plotted as a function of time for a Grashof number of 10^6. No more than some 5 dimensionless time units $\tilde{h}/\tilde{u}_b$ are needed to establish a constant speed of propagation in this case. However, for a phase of constant speed to develop, the Reynolds (or Grashof) number of the flow must be sufficiently high, since viscous friction retards the front substantially at lower Re. Figure 3 also gives the front speed for a flow at $Gr = 3 \times 10^4$, where it is seen that u_f continuously decreases after the initial transient. Consequently, the Reynolds number also drops with time and remains well below 100 after $t = 5$, say. In this case no translating frame of reference

Gr	Re	(x_1^l, x_3^l)	(x_1^u, x_3^u)
3×10^4	< 100	$(-0.64, -1.0)$	(1.9, 0.72)
9×10^4	~ 170	$(-0.6, -1.0)$	(1.6, 0.22)
10^6	~ 650	$(-0.38, -1.0)$	(1.54, 0.35)
10^7	~ 2100	$(-0.18, -1.0)$	(0.95, −0.43)
4×10^8	~ 14000	$(-0.023, -1.0)$	(0.24, −0.84)

TABLE 1. Grashof and Reynolds numbers of the two-dimensional base flows examined in the stability analysis. (x_1^l, x_3^l) and (x_1^u, x_3^u) are the coordinates of the respectively lower-left and upper-right corner of the rectangular subdomain used in the analysis (see figure 4).

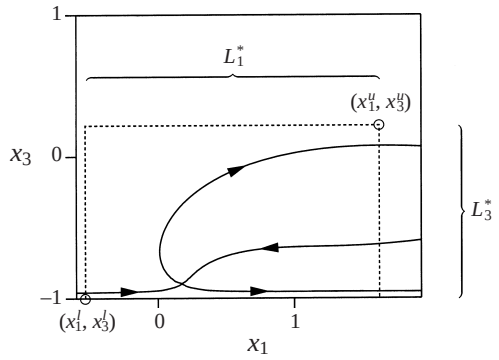

FIGURE 4. Structure of the foremost part of a gravity current at $Gr = 9 \times 10^4$ visualized by the stagnation streamline in the translating system (arrows indicate the flow direction). The subdomain of size $L_1^* \times L_3^*$ used in the linear-stability analysis is shown by the dashed rectangle. The lower boundary of the subdomain coincides with the bottom wall, and its lower-left and upper-right corners (coordinates (x_1^l, x_3^l) and (x_1^u, x_3^u), respectively) are enclosed by circles.

exists in which the flow at the head is stationary; however, we have still performed a stability analysis for this flow using the DNS results at $t = 10$. The instantaneous front speed at this time was then employed as the translational velocity of the moving frame of reference.

In the present stability analysis, we examine flows at five different Grashof numbers which are summarized in table 1 together with the respective Reynolds numbers. The second smallest Grashof number 9×10^4 is large enough to allow a constant-speed phase to develop; however, this flow differs from the flows at higher Gr in that the Grashof number is still below the threshold where the primary two-dimensional instability of the flow sets in which leads to the formation of Kelvin–Helmholtz-like billows at the interface (Härtel & Meiburg 1999). For the stability analysis, flow fields were taken typically some 9 to 12 dimensionless time units after the initial release. At this time the flow at the foremost part of the front is fully developed.

The topology of the head of a lock-exchange gravity current is illustrated in figure 4 where the flow field for $Gr = 9 \times 10^4$ is visualized by the stagnation streamline in a frame of reference moving with the head. The translating coordinate system in figure 4 is chosen such that the x_3-axis is at the nose of the head, i.e. at the foremost point. The horizontal axis x_1 is in the centre of the channel, meaning that the walls are located at $x_3 = \pm 1$. Among the distinct features of the flow at the head which are visible from figure 4, is the thin layer of light fluid which is pulled beneath the head as a consequence of the no-slip condition at the lower boundary. The nose of the

front is seen to be raised some distance above the wall, and the streamline pattern shows that the stagnation point in the translating system is located below and slightly behind the nose in the vicinity of the wall. This feature of the flow topology is of special interest with regard to the frontal instability, since it gives rise to a region of unstably stratified fluid between stagnation point and nose which does not involve the light fluid overrun by the front. As we pointed out in Part 1, this structure is also observed at the head of three-dimensional fronts even though the presence of the lobes and clefts strongly affects the flow pattern locally. Still, the mean flow topology of a three-dimensional front, obtained for example by averaging the flow in spanwise direction, is very similar to what is seen for the purely two-dimensional front in figure 4.

Finally, we note that the extent of the region around the head where stationary conditions are encountered depends on the Reynolds number. The fact that at too low Reynolds numbers no truly steady-state flow at the head develops has already been discussed. On the other hand, due to the developing two-dimensional Kelvin–Helmholtz-like instability at the interface, the stationary flow region at the head shrinks continuously with increasing Reynolds number, since the location where this instability first appears moves progressively towards the nose. However, the immediate neighbourhood of the nose and stagnation point does remain stationary in the translating system for two-dimensional fronts up to Reynolds numbers of at least 30 000, as shown in Part 1.

4. Linear stability analysis

The stability analysis concentrates on the flow at the leading edge of the front where both experiments and DNS indicate the primary instability sets in. As is common in linear stability theory (see Drazin & Reid 1981), we employ a decomposition of the flow variables into a mean-flow component and a (infinitesimally) small disturbance. In the present case the mean-flow component is the two-dimensional, steady-state flow at the foremost part of the gravity current, while the disturbance is assumed to be three-dimensional. If the mean-flow part is indicated by an overbar and the disturbance by a prime, this decomposition is

$$u_i(x_i, t) = \bar{u}_i(x_1, x_3) + u_i'(x_1, x_2, x_3, t), \tag{4}$$

$$p(x_i, t) = \bar{p}(x_1, x_3) + p'(x_1, x_2, x_3, t), \tag{5}$$

$$\rho(x_i, t) = \bar{\rho}(x_1, x_3) + \rho'(x_1, x_2, x_3, t). \tag{6}$$

For the disturbance we employ an ansatz which is largely guided by the appearance of the frontal breakdown as depicted in figure 2, which suggests that the relevant primary instability is an absolute instability in the moving frame of reference (see Huerre & Monkewitz 1990). Moreover, we infer from the formation of the regularly-spaced filaments that this instability is wave-like in the spanwise direction, with some wavenumber β, and that it is stationary in the sense that it does not travel along the leading edge. Finally, since we are dealing with a linear analysis, we assume that the dominant mode grows (or decays) exponentially with time at a rate σ. These assumptions correspond to the following general form of the disturbances:

$$f' = \hat{f}(x_1, x_3)\cos(\beta x_2)\mathrm{e}^{\sigma t} \quad \text{for} \quad f' = u_1', u_3', p', \rho', \tag{7}$$

$$f' = \hat{f}(x_1, x_3)\sin(\beta x_2)\mathrm{e}^{\sigma t} \quad \text{for} \quad f' = u_2', \tag{8}$$

where $\hat{f}$ is the amplitude function (or shape function) that does not depend on time. Note that for continuity u_2' must be expressed as a sine, if cosines are employed for the other two velocity components. To obtain the evolution equations for the disturbance part, (4)–(8) must be inserted into the basic equations (1)–(3), and the mean-flow equations, which are assumed to be fulfilled, have to be subtracted. If, furthermore, all terms which are quadratic in the disturbances are neglected, the following system of linear partial differential equations is obtained:

$$\frac{\partial \hat{u}_1}{\partial x_1} + \beta \hat{u}_2 + \frac{\partial \hat{u}_3}{\partial x_3} = 0, \tag{9}$$

$$\sigma \hat{u}_1 + \hat{u}_1 \frac{\partial \bar{u}_1}{\partial x_1} + \hat{u}_3 \frac{\partial \bar{u}_1}{\partial x_3} + \bar{u}_1 \frac{\partial \hat{u}_1}{\partial x_1} + \bar{u}_3 \frac{\partial \hat{u}_1}{\partial x_3} + \frac{\partial \hat{p}}{\partial x_1} = \frac{1}{\sqrt{Gr}} \left(\frac{\partial^2 \hat{u}_1}{\partial x_1^2} - \beta^2 \hat{u}_1 + \frac{\partial^2 \hat{u}_1}{\partial x_3^2} \right), \tag{10}$$

$$\sigma \hat{u}_2 + \bar{u}_1 \frac{\partial \hat{u}_2}{\partial x_1} + \bar{u}_3 \frac{\partial \hat{u}_2}{\partial x_3} - \beta \hat{p} = \frac{1}{\sqrt{Gr}} \left(\frac{\partial^2 \hat{u}_2}{\partial x_1^2} - \beta^2 \hat{u}_2 + \frac{\partial^2 \hat{u}_2}{\partial x_3^2} \right), \tag{11}$$

$$\sigma \hat{u}_3 + \hat{u}_1 \frac{\partial \bar{u}_3}{\partial x_1} + \hat{u}_3 \frac{\partial \bar{u}_3}{\partial x_3} + \bar{u}_1 \frac{\partial \hat{u}_3}{\partial x_1} + \bar{u}_3 \frac{\partial \hat{u}_3}{\partial x_3} + \frac{\partial \hat{p}}{\partial x_3} = \frac{1}{\sqrt{Gr}} \left(\frac{\partial^2 \hat{u}_3}{\partial x_1^2} - \beta^2 \hat{u}_3 + \frac{\partial^2 \hat{u}_3}{\partial x_3^2} \right) - \hat{\rho}, \tag{12}$$

$$\sigma \hat{\rho} + \hat{u}_1 \frac{\partial \bar{\rho}}{\partial x_1} + \hat{u}_3 \frac{\partial \bar{\rho}}{\partial x_3} + \bar{u}_1 \frac{\partial \hat{\rho}}{\partial x_1} + \bar{u}_3 \frac{\partial \hat{\rho}}{\partial x_3} = \frac{1}{\sqrt{Gr\, Sc^2}} \left(\frac{\partial^2 \hat{\rho}}{\partial x_1^2} - \beta^2 \hat{\rho} + \frac{\partial^2 \hat{\rho}}{\partial x_3^2} \right). \tag{13}$$

The system (9)–(13) constitutes an eigenvalue problem where $\hat{u}_i$, $\hat{\rho}$, and $\hat{p}$ are the eigenfunctions and σ is the eigenvalue that depends on β and Gr. In general, σ may also be a function of the Schmidt number, which is very large (typically $O(10^3)$) in experiments where salt water and fresh water are used as working fluids. On the other hand, in intrusion flows of gas mixtures, where the same frontal instabilities occur, Schmidt numbers are usually of order one. From a precursor study we found that the dependence of σ on Sc is indeed weak unless Sc becomes very small, and therefore we have restricted the analysis to Schmidt numbers of unity here.

4.1. *Computational approach*

To solve the eigenvalue problem we employ a collocation technique, where the stability equations are discretized in a rectangular subdomain of size $L_1^* \times L_3^*$ that encompasses the foremost part of the front. The size of the subdomain and its location were chosen such that the flow region where the relevant eigenfunctions are most pronounced is captured well. For illustration, the subdomain used in the analysis of the flow at $Gr = 9 \times 10^4$ is depicted in figure 4 as a dashed rectangle. The length and height of the subdomain are $L_1^* = 2.2$ and $L_3^* = 1.22$, respectively, in this case. The spatial discretization within the subdomain is performed on an equidistant mesh with nodal points that are at the same locations as the corresponding nodes of the computational grid used in the DNS of the base flow. A highly-accurate compact finite difference scheme of at least sixth-order according to Lele (1992) is applied to discretize the spatial derivative operators. This transforms the set of stability equations into a general algebraic eigenvalue relation of the form

$$\boldsymbol{A}\boldsymbol{\phi} = \sigma \boldsymbol{B}\boldsymbol{\phi}, \tag{14}$$

where $\boldsymbol{A}$ and $\boldsymbol{B}$ are $N \times N$ non-sparse matrices that contain the coefficients of the differentiation schemes and the coupling terms between the five discretized budget equations (see Carlsson & Thunblom 1998). $\boldsymbol{\phi}$ is the vector that is composed of the nodal-point values of the amplitude functions $\hat{u}_i$, $\hat{p}$, and $\hat{\rho}$. The number of nodal

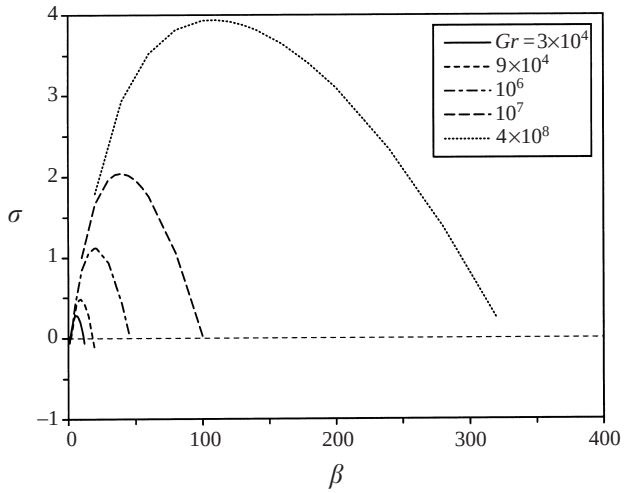

FIGURE 5. Stability diagram of the flow at a gravity-current head. Shown is the amplification rate σ of the first mode of instability as a function of wavenumber β and Grashof number Gr.

points, and hence the size of the system (14), depends on the extent of the subdomain and the computational resolution employed. In the present study, between several hundred and 2700 nodal points were used within the subdomain, giving a maximum size of $N = 13\,500$ for the matrices $\boldsymbol{A}$ and $\boldsymbol{B}$.

Since we are primarily interested in the dominant modes of instability, the complete spectrum of the generalized eigenvalue problem does not need to be evaluated. Therefore, we have employed an iterative procedure based on the implicitly restarted Arnoldi method (Sorensen 1992) to solve (14) for the leading eigenvalues. In the computational implementation of the eigenvalue solver we have made use of the subroutine system ARPACK (see Maschhoff & Sorensen 1996). After each iteration step, the accuracy of the eigenvalues and eigenvectors was tested by computing the residual $r \equiv ||\boldsymbol{A}\boldsymbol{\phi} - \sigma\boldsymbol{B}\boldsymbol{\phi}||$, and the iteration was terminated when the convergence criterion $r < 10^{-10}$ was met.

From figure 4 it is seen that the subdomain has open boundaries at the top and at both sides, and at these locations no natural boundary conditions for the amplitude functions are available. However, from our analysis we found that the eigenvalues and the associated eigenfunctions are not very sensitive to the boundary conditions chosen, provided the subdomain is sufficiently large to accommodate the regions where the amplitude functions are most pronounced. All results presented here were obtained with homogeneous Neumann conditions for the disturbances at the open boundaries, meaning that the gradients of the disturbance quantities normal to the respective boundaries are required to vanish. At the rigid bottom wall, on the other hand, homogeneous Dirichlet conditions for the velocities and homogeneous Neumann conditions for the density are the natural choice.

4.2. *Discussion of the stability results*

The key finding of our present analysis is that the head of a gravity current is linearly unstable to three-dimensional disturbances throughout the range of Grashof numbers examined. The stability diagram of the flow is shown in figure 5 where the growth rate σ of the instability is displayed as a function of β and Gr. Only results for the first mode of instability are shown in figure 5, although at times more than

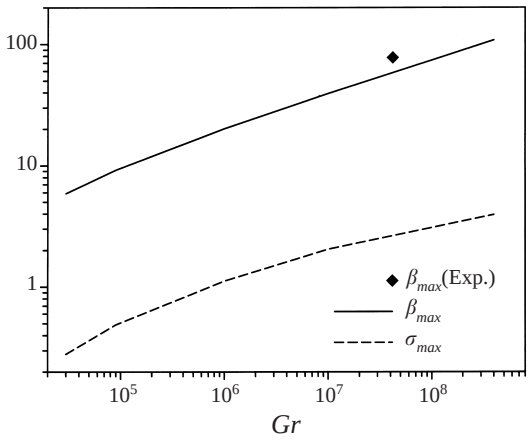

FIGURE 6. Wavenumber β_{max} and amplification rate σ_{max} of the most unstable mode as function of Grashof number. The experimental data point is extracted from Simpson (1972) (see figure 2).

one unstable mode was obtained from the analysis. However, in all cases the higher modes of instability were insignificant, since their associated amplification rates were much smaller than those of the first mode. Particularly noteworthy is the fact that even for the two smallest Grashof numbers unstable three-dimensional modes can be found. This shows that the first instability to be observed at a gravity-current head is a three-dimensional one, since at such low Grashof numbers no two-dimensional Kelvin–Helmholtz-like rollers form. It is seen from the stability diagram that the amplification rates strongly increase with Grashof number. For $Gr = 4 \times 10^8$, for example, growth rates can become as large as 4, meaning that disturbance amplitudes will grow by more than a factor of 50 within a single dimensionless time unit. This suggests that the breakdown of an essentially two-dimensional flow front would occur very abruptly at high Reynolds numbers, a fact that may render it difficult to monitor and analyse the primary instability experimentally in this case, even under carefully controlled conditions.

The stability diagram makes clear that the range of wavenumbers for which unstable modes appear, broadens substantially with increasing Grashof number, although the minimum wavenumber below which no unstable modes exist is similar for all Gr. The curves in figure 5 feature distinct maxima which indicate that at each Grashof number a most amplified disturbance exists, that we will generally refer to as the most unstable mode in the remainder of this paper. The associated amplification rate and the spanwise wavenumber of this mode will be denoted as σ_{max} and β_{max}, respectively. The variation of β_{max} and σ_{max} with Grashof number, as extracted from the stability diagram, is shown in figure 6. At $Gr = 3 \times 10^4$ the maximum amplification rate occurs for $\beta \approx 6$, which corresponds to a wavelength $\lambda = 2\pi/\beta$ approximately equal to the height of the gravity-current head; however, the wavelength of the most unstable mode decreases to only little more than $\frac{1}{20}$ at $Gr = 4 \times 10^8$. To compare the present findings with experiments, we have determined β_{max} from the spacing of the initial filaments in Simpson's sketch in figure 2. The result is included in figure 6 and it is seen to agree well with the predictions from the linear-stability analysis. However, a more detailed comparison with laboratory measurements over a range of Reynolds numbers would certainly be desirable, but to our knowledge no further quantitative results on the initial filamentary structure are available from published laboratory

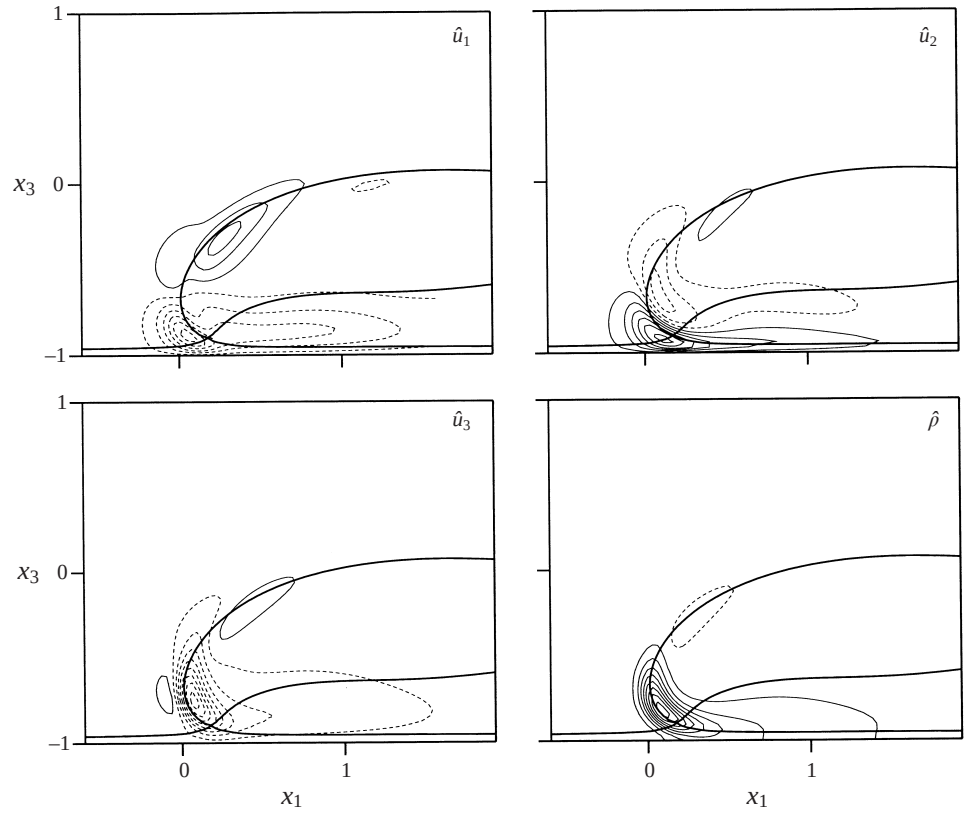

FIGURE 7. Isocontours of the amplitude functions of the most unstable mode for $Gr = 9 \times 10^4$. Solid and dashed lines represent positive and negative values, respectively. The thick solid line is the stagnation streamline.

experiments at present. A more thorough validation can therefore only be achieved by comparison with direct numerical simulations of the early stages of the frontal breakdown. This will be done in the next section.

The spatial structure of the leading-edge instability is visualized in figure 7 where the amplitude functions $\hat{u}_1$, $\hat{u}_2$, $\hat{u}_3$, and $\hat{\rho}$ of the most unstable mode are depicted for the flow at $Gr = 9 \times 10^4$. It is seen that the instability is most pronounced at the foremost part of the head. All disturbance components have their peaks in the region around the leading edge and decay quickly with increasing distance from the nose. The localization of the instability at the leading edge of the front is even more pronounced at higher Grashof numbers. This is illustrated by figure 8 which gives the amplitude functions of the respective most unstable modes at different Gr. For simplicity, only $\hat{u}_2$ is shown in the figure, but very similar results are obtained for the other disturbance components. The region primarily affected by the leading-edge instability is located between stagnation point and nose, and shrinks substantially with increasing Gr. We remark that, although the stagnation point approaches the wall for increasing Grashof number (see table 1 of Part 1), the Reynolds number of the near-wall flow, formed in terms of the height of the stagnation point, still grows. Consequently, the stabilizing effect of viscous forces quickly diminishes with increasing Grashof number, a fact that is reflected by the increase of σ with Gr seen in figure 5.

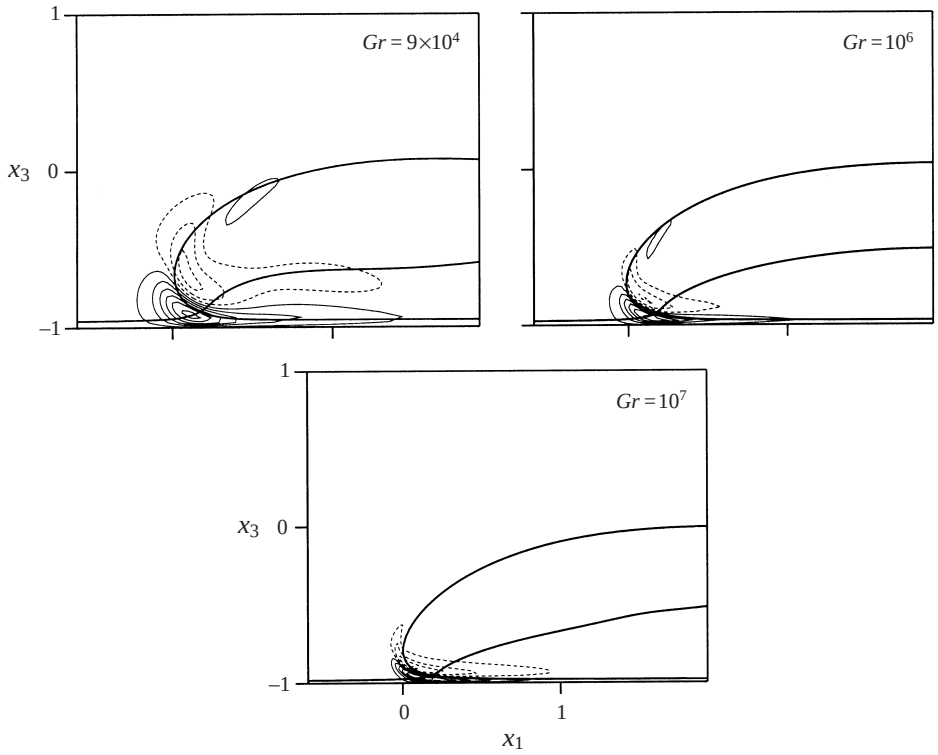

FIGURE 8. Structure of the respective most unstable modes at different Grashof numbers. Shown are isocontours of the amplitude function $\hat{u}_2$. Solid and dashed lines indicate positive and negative values, respectively. In each picture the thick solid line is the stagnation streamline.

Because the eigenfunctions become more and more localized, we could use much smaller subdomains in the analysis of flows at higher Grashof numbers. Table 1 gives the coordinates (x_1^l, x_3^l) and (x_1^u, x_3^u) of the respectively lower-left and upper-right corner of the subdomain used for the different Gr. It is seen that the area that the analysis window covers differs by more than a factor of 100 between the lowest and highest Grashof number examined; however, the total number of nodal points in the analysis window, and hence the numerical expense of the stability analysis, still grows with increasing Grashof number, since the spatial discretization must be drastically refined with increasing Gr.

The fact that the eigenfunctions are most pronounced in the unstably stratified region between stagnation point and nose suggests that the frontal instability is caused by buoyancy forces. To examine more specifically the role that buoyancy plays, we have repeated part of the analysis using simplified stability equations in which the gravity term was dropped (see Carlsson & Thunblom 1998). In this case no unstable modes could be found, which provides evidence that the mechanism triggering the breakdown of the front into the lobe-and-cleft pattern is indeed a gravitational instability. However, the instability shown in figures 7 and 8, which acts in a localized way at the leading edge, is not related to the unstable stratification between the heavy fluid within the head and the thin layer of light fluid that the front overruns (note that the light fluid in the region between the nose and stagnation point resides only temporarily underneath the front, but eventually flows above the head). Since this thin layer of light fluid underneath the front has been thought to

be held responsible for the frontal instability in the past, we have also examined the stability properties of the near-wall flow beneath the head using an appropriately modified observation window. The analysis showed that in this flow region further gravitational instabilities may indeed exist, but their contribution to the frontal breakdown is negligible, since they are much less amplified than the most unstable mode at the leading edge (Carlsson & Thunblom 1998).

5. Direct numerical simulations

Sufficiently detailed experimental results on the frontal instability are not available at present, and therefore we performed direct numerical simulations of three-dimensional lock-exchange flows for comparison with the results from our linear-stability analysis. In addition to validating the stability computations for the leading edge, the DNS also serve to clarify whether or not further three-dimensional instabilities exist in the flow. Note that our linear-stability analysis not only has focused on small subdomains at the head, but also that the ansatz (7), (8) for the disturbances would miss travelling modes or spatially growing instabilities. For the simulations the code of Härtel *et al.* (1997) was employed, which is based on a mixed spectral/spectral-element discretization in space along with finite differences in time. In the DNS, minute three-dimensional disturbances with amplitudes of the order of 10^{-12} were superimposed on the initial flow field, and their evolution with time was monitored. The disturbance field was essentially random, but constructed in such a manner that it features a broad and flat spectrum which includes the most unstable mode from the stability analysis of the two-dimensional flow at the respective Grashof number. The width L_2 of the box was generally larger (typically 4–5 times larger) than the wavelength of the most unstable mode in order to avoid the disturbance spectrum being confined to this mode and its higher harmonics.

Three different Grashof numbers were considered for comparison with the stability analysis, namely 3×10^4, 10^6, and 10^7. The rather low Grashof number of 3×10^4, which is below the threshold where a phase of constant speed of propagation develops (see figure 3), was chosen to probe the robustness of the linear-stability results. Recall that at this Grashof number the requirement of stationary conditions at the foremost part of the front is not fully satisfied. From the DNS results, the eigenfunctions (modes) associated with a given spanwise wavenumber β are readily obtained by a Fourier transformation of the velocity components and the pressure. For example, the component $\hat{u}_2$ of the eigenfunction is given by

$$\hat{u}_2(x_1, \beta, x_3, t) = \frac{2}{\pi} \int_0^{L_2} u_2(x_1, x_2, x_3, t) \sin(\beta x_2)\, \mathrm{d}x_2. \tag{15}$$

Since the spanwise velocity component u_2 vanishes for strictly two-dimensional flows, it can be employed to measure directly the three-dimensionality of the flow.

A first impression of the temporal evolution of small three-dimensional disturbances in lock-exchange flow can be gained from figure 9 where the time history is given of the maximum of u_2 (normalized by its initial value) for all three Grashof numbers. The curves in figure 9 show that from about $t = 3$–4 on, an exponential growth of the disturbance amplitudes sets in which indicates that the flows are linearly unstable. More detailed insight into the evolution of the instability is achieved by considering the spanwise spectra of the velocity component u_2. Figure 10 shows such spectra as a function of spanwise wavenumber β for five successive times of the simulations which are increments of two non-dimensional time units apart. The curves represent

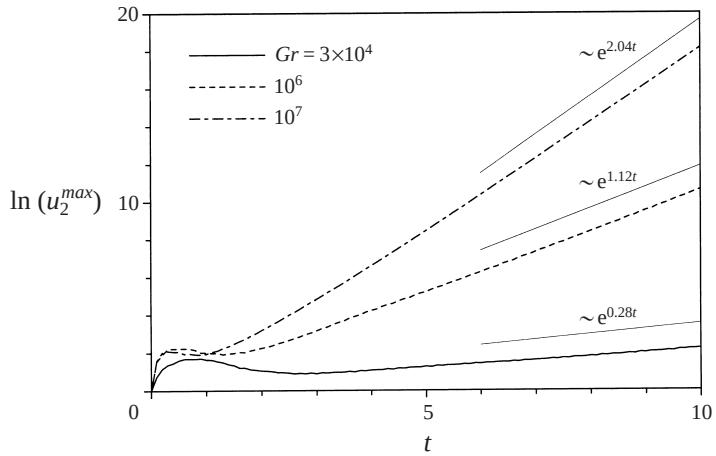

FIGURE 9. Temporal development of the amplitude of three-dimensional disturbances in direct numerical simulations of lock-exchange flows. The curves give the maximum of u_2 over the whole flow domain, normalized by the maximum of the initial random disturbance at $t = 0$. The thin lines indicate the theoretical growth of the most unstable modes according to linear-stability analysis (see table 2).

the maximum $\hat{u}_2^m$ of each mode over the (x_1, x_3)-plane, i.e.

$$\hat{u}_2^m(\beta, t) = \max_{x_1, x_3}\{\hat{u}_2(x_1, \beta, x_3, t)\}. \tag{16}$$

For the Grashof numbers 3×10^4 and 10^6 the agreement with the stability diagram in figure 5 is striking. Except for modes with very small wavenumbers and for very early times, the growth and decay of the individual disturbance components agrees closely with the linear analysis. For each β, the logarithm of the disturbance amplitude in essence grows linearly with time at a rate equal to the amplification rate σ of the first mode of instability depicted in figure 6. We have evaluated the actual growth rates by taking the ratio of amplitudes at times $t = 8$ and 10, and the results obtained for the respective most unstable modes are compared with the predictions from linear-stability theory in table 2. For both Grashof numbers the difference amounts to a few per cent only. It is remarkable that even for the smallest Grashof number the DNS result agrees well with the stability analysis, despite the fact that steady-state conditions at the head of the front are not attained. The associated amplitude functions $\hat{u}_2$ and $\hat{\rho}$ of the fastest growing modes are displayed in figures 11 and 12 for the Grashof numbers 3×10^4 and 10^6. For comparison, the corresponding results from the linear-stability analysis for the same spanwise wavenumber are included in the figures, and again an excellent agreement is seen. These results make clear that in a spatially and temporally developing lock-exchange flow, the dominant mode of instability is indeed the most unstable mode that a local linear stability analysis of the flow at the foremost part of the front predicts.

The results for $Gr = 10^7$ shown in figure 10 differ slightly from what is seen for the two lower Grashof numbers, in that the stability properties of the flow during the initial transient lead to a stronger excitation of higher modes within the first 2–4 dimensionless time units. However, once the flow at the head is fully developed, the amplification rates approach the values obtained from the linear-stability analysis,

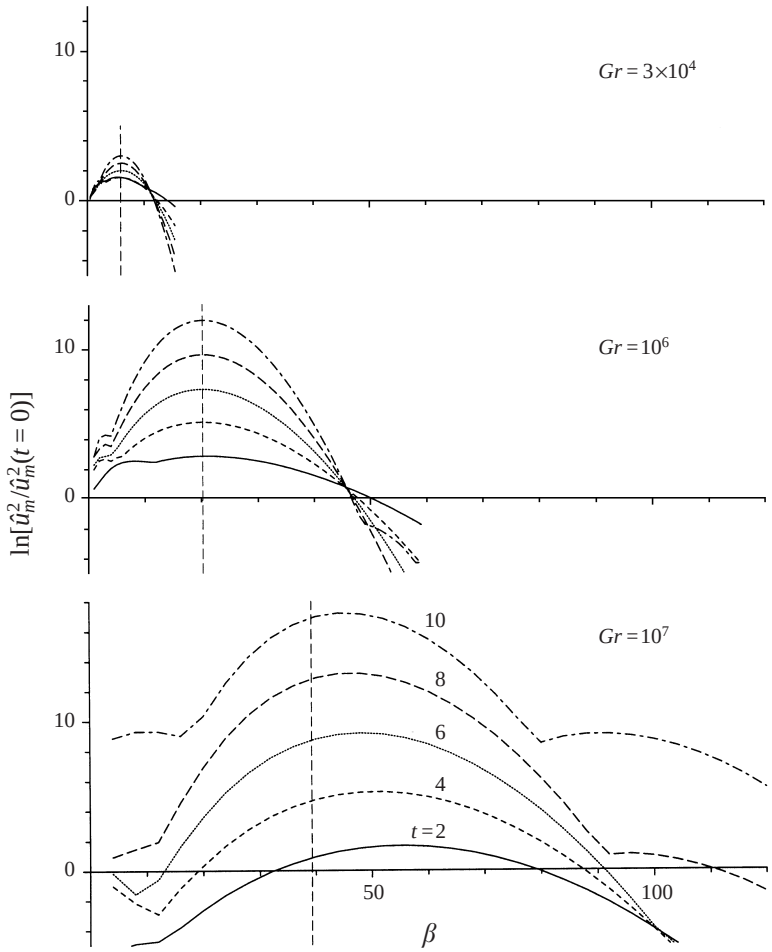

FIGURE 10. Spanwise spectra of the velocity component u_2 (see equation (16)) obtained from DNS at three different Grashof numbers (results are normalized by the respective values at $t = 0$). Given are results for five successive times of the simulations two time units apart. The flow fields were initialized with random disturbances with a maximum amplitude of the order of 10^{-12}. The wavelengths of the most-unstable modes according to linear-stability theory are indicated by the dashed vertical lines.

and this causes the peak in the spectrum to move towards the wavenumber of the most unstable mode according to figure 6. Note that the most-amplified mode at a given time cannot be deduced from the maximum in the disturbance spectrum, since the actual amplitude of a mode depends on the entire time history of the flow. Like for the two lower Grashof numbers, we have computed the amplification rate for $Gr = 10^7$ from the increase in amplitude between times $t = 8$ and 10, and again achieved close agreement with the linear-stability analysis concerning both the spanwise wavelength of the most unstable mode and its actual amplification rate. The comparison of σ_{max} with the linear-stability result is included in table 2 where it is seen that the two agree to at least three digits.

As a final remark we point out that for $Gr = 10^7$ the strongly increasing amplitudes seen at both the low- and high-wavenumber part of the spectrum at later times do not

Gr	σ_{max}^{LST}	σ_{max}^{DNS}	ε
3×10^4	0.28	0.26	$\approx 7\%$
10^6	1.12	1.14	$\approx 2\%$
10^7	2.04	2.04	$< 0.5\%$

TABLE 2. Amplification rate σ of small three-dimensional disturbances with a lateral wavenumber of β_{max} according to figure 6. Comparison of DNS results and linear-stability theory (LST) for different Grashof numbers. ε is the relative difference in the results related to the value obtained from the DNS.

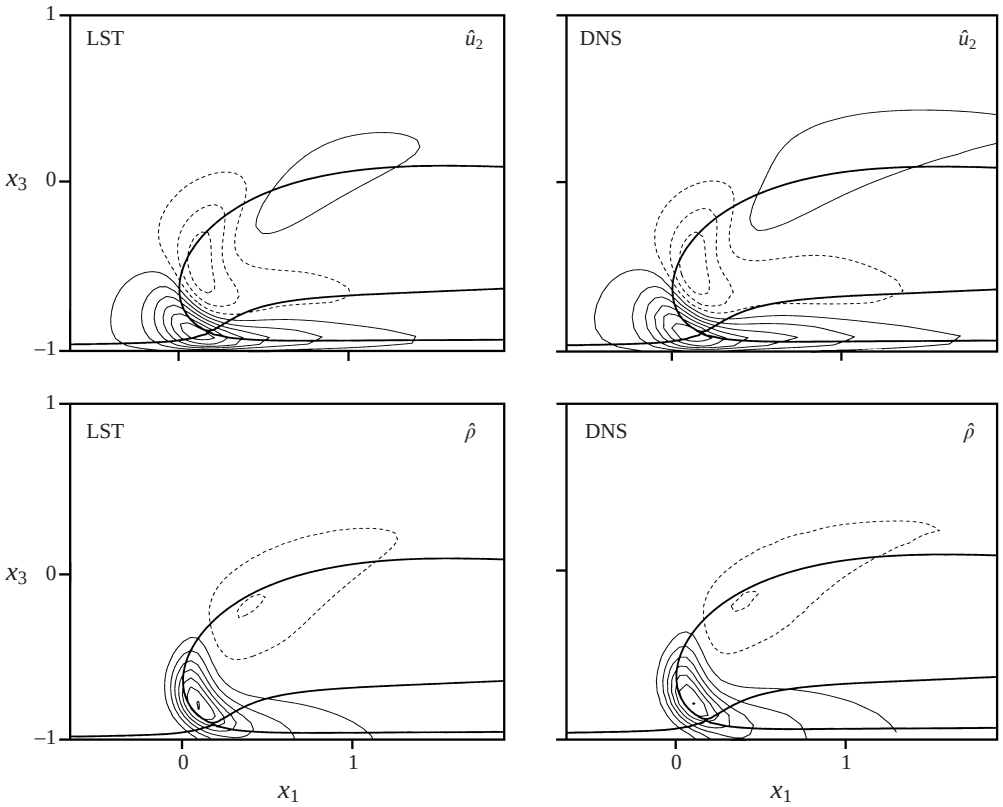

FIGURE 11. Isocontours of the amplitude functions $\hat{u}_2$ and $\hat{\rho}$ of the most unstable mode for $Gr = 3 \times 10^4$. Comparison of results from linear-stability theory (LST) and DNS.

indicate the onset of another type of instability. Since the growth rates of the most unstable modes are very large at this Grashof number, the dominant disturbance amplitudes rise by 7–8 orders of magnitude within the first 10 dimensionless time units, meaning that the maxima of the respective eigenfunctions have already grown to about 10^{-5} or even 10^{-4}. Consequently, nonlinear interactions of these modes excite disturbances at the lower and upper ends of the spectrum, the amplitudes of which scale with approximately the square of the amplitude of the primary disturbances. At later times these 'passive' modes become visible as pronounced wings in the disturbance spectrum in figure 10.

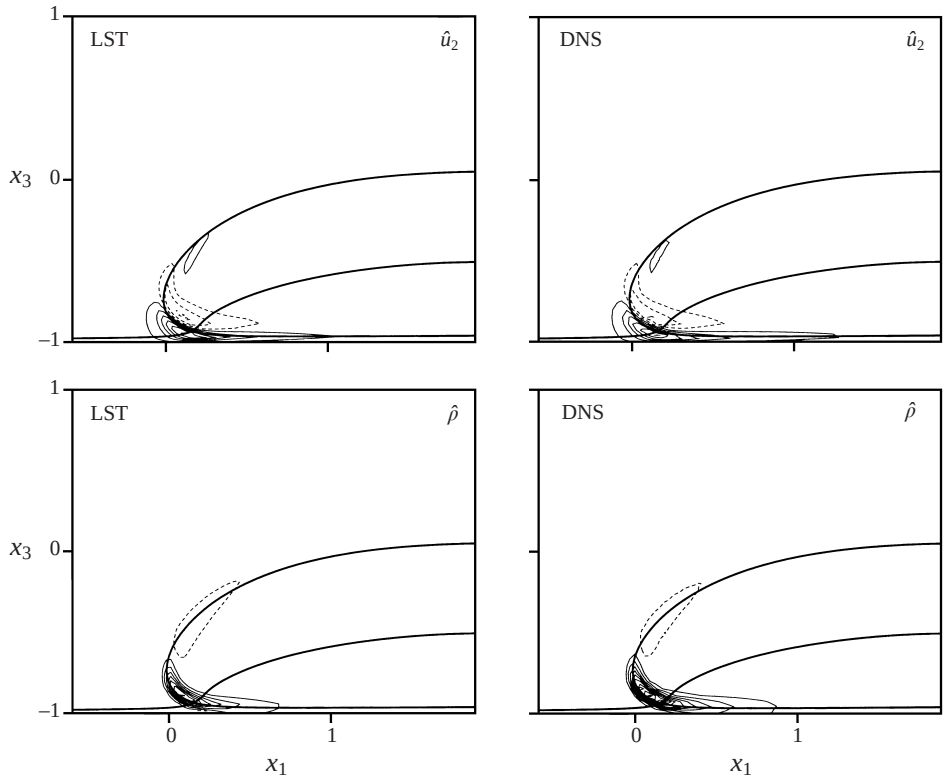

FIGURE 12. Isocontours of the amplitude functions $\hat{u}_2$ and $\hat{\rho}$ of the most unstable mode for $Gr = 10^6$. Comparison of results from linear stability theory (LST) and DNS.

6. Concluding remarks

In the present paper we have clarified the long-standing issue of the nature of the hydrodynamic instability that initiates the breakdown of a flow front into the lobe-and-cleft structure. Experiments have shown that the transition from an essentially two-dimensional front into a highly irregular three-dimensional state passes through distinct stages, the first of which being characterized by the development of a regular filamentary structure at the leading edge. We have conducted a linear-stability analysis of the flow at the foremost part of the front which reveals that the spacing of the initial filaments is closely related to the preferred wavelength of a vigorous instability that has not been recognized before. The stability analysis was based on DNS data of two-dimensional mutual intrusion flows, but only a small subdomain enclosing the foremost part of the front was considered. A wave ansatz for the disturbances was used, and the resulting generalized eigenvalue problem for the temporal growth rate of the most unstable modes was solved numerically. From the associated eigenfunctions it became clear that the frontal instability is not caused by overrun light fluid, as assumed in the past; rather it is due to the unstable stratification that prevails at the leading edge between the nose and stagnation point of the front.

At present, no sufficiently detailed experimental data are available that could be used for comparison with our linear-stability analysis. Therefore, we have also presented three-dimensional direct simulations of the early stages of the frontal breakdown in this paper, in order to validate the findings from the stability calculations.

In the simulations the flow fields were initialized with minute random disturbances, but after a short initial transient the disturbance spectrum was found to develop in line with what the linear-stability analysis of the flow at the head predicts. An excellent agreement was obtained not only with respect to the preferred wavelength of the instability, but also concerning the spatial structure and the temporal growth rate of the respective most unstable modes. Note that in the direct simulations the full spatial and temporal development of the frontal system is taken into account; however, no relevant three-dimensional instabilities were observed other than those predicted by the local stability analysis of the region around the nose of the front. It is clear, therefore, that the development of the three-dimensionality in the flow is determined by the conditions at the head where the dominant instability is localized.

Most of the present work was conducted while F. C. and M. T. were guests at the Institute for Fluid Dynamics of ETH Zürich. The authors wish to thank Professor L. Löfdahl and Dr J. P. Kunsch for their support which made this joint project possible. The authors also wish to thank M. Ballabio for optimizing the DNS code for the NEC SX-4 system at CSCS, Manno. Helpful comments by Dr A. Bakchinov and F. Necker on a previous version of this paper are gratefully acknowledged.

REFERENCES

Britter, R. E. & Simpson J. E. 1978 Experiments on the dynamics of a gravity current head. *J. Fluid Mech.* **88**, 223–240.

Carlsson, F. & Thunblom, M. 1998 Analysis of three-dimensional instabilities at a gravity-current head. Diploma Thesis, ETH Zürich/Chalmers University of Technology, Gothenburg, Sweden.

Drazin, P. G. & Reid, W. H. 1981 *Hydrodynamic Stability*. Cambridge University Press.

Gebhart, B., Jaluria, Y., Mahajan, R. L. & Sammakia, B. 1979 *Buoyancy-Induced Flows and Transport*. Hemisphere.

Hallworth, M. A., Huppert, H. E., Phillips, J. C. & Sparks, S. J. 1996 Entrainment into two-dimensional and axisymmetric turbulent gravity currents. *J. Fluid Mech.* **308**, 289–311.

Härtel, C., Kleiser, L., Michaud, M. & Stein, C. F. 1997 A direct numerical simulation approach to the study of intrusion fronts. *J. Engng Maths* **32**, 103–120.

Härtel, C. & Meiburg, E. 1999 Gravity currents and their analysis by direct numerical simulation. *Fortschritt-Bericht* 366. VDI Verlag, Düsseldorf.

Härtel, C., Meiburg, E. & Necker, F. 2000 Analysis and direct numerical simulation of the flow at a gravity-current head. Part 1. Flow topology and front speed for slip and no-slip boundaries. *J. Fluid Mech.* **418**, 189–212.

Huerre, P. & Monkewitz, P. A. 1990 Local and global instabilities in spatially developing flows. *Ann. Rev. Fluid Mech.* **22**, 473–537.

Lele, S. K. 1992 Compact finite difference schemes with spectral-like resolution. *J. Comput. Phys.* **103**, 16–42.

Maschhoff, K. J. & Sorensen, D. C. 1996 P-ARPACK: An efficient portable large scale eigenvalue package for distributed memory parallel architectures. In *Applied Parallel Computing in Industrial Problems and Optimization* (ed J. Wasniewski *et al.*), Lecture Notes in Computer Science 1184, Springer.

Simpson, J. E. 1969 A comparison between laboratory and atmospheric density currents. *Q. J. R. Met. Soc.* **95**, 758–765.

Simpson, J. E. 1972 Effects of the lower boundary on the head of a gravity current. *J. Fluid Mech.* **53**, 759–768.

Simpson, J. E. 1997 *Gravity Currents: in the Environment and the Laboratory* 2nd Edn. Cambridge University Press.

Sorensen, D. C. 1992 Implicit application of polynomial filters in a k-step Arnoldi method. *SIAM J. Matrix Anal. Applics* **13**, 357–385.